

Investigation of LaFeO₃ perovskite growth mechanism through mechanical ball milling of lanthanum and iron oxides

Monica Sorescu · Tianhong Xu · Johanna D. Burnett · Jennifer A. Aitken

Received: 22 March 2011 / Accepted: 9 May 2011 / Published online: 18 May 2011
© Springer Science+Business Media, LLC 2011

Abstract LaFeO₃ perovskite was synthesized mechanochemically through ball milling of La₂O₃ and Fe₂O₃ in stoichiometric ratio. X-ray powder diffraction (XRPD), simultaneous differential scanning calorimetry and thermogravimetry analysis (DSC-TGA), Mössbauer spectroscopy, scanning electron microscopy (SEM), and optical diffuse reflectance spectroscopy were combined for a detailed study of the growth mechanism of LaFeO₃ perovskite during the ball milling process. The XRPD results showed that La₂O₃ is unstable when exposed to air. Both La₂O₃ and La(OH)₃ phases coexist under the ball milling process, indicating that La₂O₃ or La(OH)₃ can be used to produce LaFeO₃. The formation of LaFeO₃ perovskite was evident after only 2 h of milling and the amount of LaFeO₃ gradually increased with the increase of ball milling time. After 12 h of ball milling, single phase LaFeO₃ was formed. The Mössbauer spectroscopy studies show that the spectrum of the formed LaFeO₃ phase consists of three sextets and one doublet, indicating the wide distribution of LaFeO₃ particle sizes and some of the smaller particles having superparamagnetic properties. This is in good agreement with the SEM images, which show that the formed LaFeO₃ phase consists of nanometer-sized particles and micrometer-sized agglomerates. The formation of LaFeO₃ phase was mainly caused by the La³⁺ substitution of Fe³⁺ in Fe₂O₃ lattice. Optical diffuse reflectance spectroscopy studies show that the formed

LaFeO₃ phase has semiconductor properties, with the band gap energy ~2.67 eV.

Introduction

ABO₃-type perovskite materials have attracted considerable attention due to their wide applications, such as catalysts [1, 2], gas sensing materials [3, 4], magnetic materials [5], fuel cell materials [6, 7], and electric ceramic materials [8, 9]. Up to now, many routes have been developed to synthesize RFeO₃-type perovskite materials (R stands for rare earth metal), such as conventional method based on the solid-state reaction between R₂O₃ and Fe₂O₃ at high temperature [10], the wet chemistry–polymerizable complex method [11, 12], and the glycine–nitrate process method [13].

In order to obtain pure LaFeO₃, it has been reported that calcinations at 1000 °C for 184 h is needed. X-ray powder diffraction patterns for shorter periods of calcinations time still show peaks of La₂O₃ and Fe₂O₃ phases, not completely reacted [14]. Even in the sonochemical method, crystalline LaFeO₃ can only be observed by calcining the precursor at 800 °C in air for 24 h. Additionally, this method utilizes expensive reactants [15]. On the other hand, the calcinations at high temperature for long periods of time decrease the surface area, which in turn limits the potential application of LaFeO₃ as catalyst. The catalytic activity and the gas sensing characteristics of LaFeO₃ are strongly dependent on the particle size [16, 17]. It has been reported that LaFeO₃ perovskite prepared by microemulsion method with smaller particle size exhibits higher catalytic activity for the NO + CO reaction than similar materials with larger particle size prepared via ceramic method [16]. The nanocrystalline LaFeO₃ shows a very

M. Sorescu (✉) · T. Xu
Department of Physics, Duquesne University, 211 Bayer Center,
Pittsburgh, PA 15282-0321, USA
e-mail: sorescu@duq.edu

J. D. Burnett · J. A. Aitken
Department of Chemistry and Biochemistry, Duquesne
University, Mellon Hall, Pittsburgh, PA 15282-1503, USA

different electrical conductivity due to the surface effect of nano-materials. The nano-LaFeO₃ displays obvious quantum confinement effects such that the density of the extrinsic surface states on the nano-material surface increases exponentially with increasing pressure of the ethanol sensor gas [17].

For catalytic applications of LaFeO₃-based materials, two factors are mainly considered, the typical crystalline structure and large surface areas. High energy ball milling is a well established method for preparing amorphous, composite, and nanocrystalline materials with high surface area and interesting defects. This preparation method is promising for use at a production scale due to its relatively low cost and simple operation.

Recently, Zhang and Saito [18] have employed the mechanochemical method to synthesize LaFeO₃ at room temperature using La₂O₃ and Fe₂O₃ as reactants. However, the magnetic properties were not studied. Cristóbal et al. [19] also synthesized the LaFeO₃ using high energy ball milling of La₂O₃ and Fe₃O₄ or Fe₂O₃. The magnetic properties of the obtained materials were measured by vibration sample magnetometry and showed a significant ferromagnetic component due to the spin-canting effect induced by the mechanochemical treatment. However, the growth mechanism of LaFeO₃ with different starting reactants (Fe₃O₄ and Fe₂O₃) was not fully discussed, and an extra step, calcinations of hygroscopic La₂O₃ at 1000 °C for 2 h, was introduced. Recently, the mechanochemical ball milling methods have been successfully employed to synthesize the LaFeO₃ perovskite oxide [20–22]. Mössbauer spectroscopy was used to characterize the magnetic properties of the as-obtained systems, especially the substitution between transition metal ions and Fe³⁺ into α-Fe₂O₃ and the transition metal oxides lattices at atomic resolution. This can provide insight into understanding the reaction mechanism of this type of solid-state reaction.

In this work, we report the successful synthesis of single phase LaFeO₃ perovskite by mechanochemical activation method through ball milling of La₂O₃–Fe₂O₃ mixtures with stoichiometric ratio at room temperature. X-ray powder diffraction, simultaneous DSC–TGA, Mössbauer spectroscopy, scanning electron microscopy, and UV–Vis spectroscopy have been employed to investigate the phase information, thermal behaviors, magnetic properties, and morphology of ball-milled oxides at different milling times. The growth mechanism of LaFeO₃ in connection with phase evolution under ball milling process is discussed.

Experimental

Lanthanum and iron oxides were commercially purchased from Alfa Aesar: lanthanum oxide (99.99% metals basis,

average particle size about 60 nm), and hematite (α-Fe₂O₃, 99% metal basis, average particle size about 48 nm). Powders of hematite and lanthanum oxides were milled at 1:1 molar ratio in a hardened steel vial with 12 stainless-steel balls (type 440; eight of 0.25 in diameter and four of 0.5 in diameter) in the SPEX 8000 mixer mill for time periods ranging from 2 to 12 h. The ball/powder mass ratio was 5:1. Prior to their introduction in the ball milling device, the powders were manually ground in air to obtain a homogeneous mixture.

The X-ray powder diffraction patterns of samples were obtained using a PANalytic X’Pert Pro MPO powder diffractometer with Cu K_α radiation (45 kV/40 mA, $\lambda = 1.54187 \text{ \AA}$) with a nickel filter on the diffracted side. A silicon-strip detector called X’cellerator was used. The scanning range was 10°–80° (2θ) with a step size of 0.02°. The average particle size was determined by the Scherrer method. The lattice parameters were extracted from Rietveld structural refinement of the XRPD patterns.

Simultaneous DSC–TGA experiments were performed using a Netzsch Model STA 449F3 Jupiter instrument with a silicon carbide (SiC) furnace. Samples were contained in an alumina crucible with an alumina lid. Series of experiments were performed using $20 \pm 2 \text{ mg}$ sample size. The atmosphere consisted of flowing protective argon gas at a rate of 50 mL/min. DSC and TGA curves were obtained by heating samples from room temperature to 800 °C with a ramp rate of 10 °C/min. Both DSC and TGA curves were corrected by subtraction of a baseline which was run under identical conditions as DSC–TGA measurement with residue of samples in the crucible. The Netzsch Proteus Thermal Analysis software was used for DSC and TGA data analysis.

Room temperature transmission Mössbauer spectra were recorded using an MS-1200 constant acceleration spectrometer with a 10 mCi ⁵⁷Co source diffused in Rh matrix. Least-squares fittings of the Mössbauer spectra were performed with the NORMOS program.

Scanning electron microscopy was performed using a Hitachi S-3400N scanning electron microscope. The powder of a 12 h ball-milled sample was adhered on top of double side carbon tape which was attached onto a standard aluminum stub and examined under high vacuum conditions. A 1.0 kV accelerating voltage and a 5.0 mm working distance were employed.

An optical diffuse reflectance spectrum was obtained using a Varian Cary 5000 UV/Vis/NIR spectrophotometer. The sample was loaded into a Harrick Praying Mantis diffuse reflectance accessory that uses elliptical mirrors. BaSO₄ was used as a 100% reflectance standard. Scans were performed from 2500 to 200 nm at a rate of 600 nm/min, wavelength data were converted to electron volts, and the percent reflectance data were converted to absorbance units using the Kubelka–Munk equation [23].

Results and discussion

X-ray powder diffraction

Figure 1 shows the evolution of XRPD patterns of mixed lanthanum and iron oxides at different ball milling times. The starting materials were pure Fe_2O_3 and La_2O_3 , however, due to the highly hygroscopic characteristics of La_2O_3 , most of the La_2O_3 converts to $\text{La}(\text{OH})_3$ when Fe_2O_3 and La_2O_3 are physically ground in air. This was confirmed by the XRPD pattern of 0 h ball-milled mixture of Fe_2O_3 and La_2O_3 (Fig. 1a). The diffraction peaks of $\text{La}(\text{OH})_3$ have much stronger intensities compared to those of the La_2O_3 phase, suggesting that $\text{La}(\text{OH})_3$ is the major phase for La-containing components and La_2O_3 is highly unstable when exposed to air. The presence of

Fe_2O_3 and absence of $\text{Fe}(\text{OH})_3$ diffraction peaks indicate that Fe_2O_3 is relatively stable in air. As expected, no diffraction peaks of LaFeO_3 phase were detected after the physically mixing process.

The appearance of the LaFeO_3 diffraction peaks (JCPDS No.: 37-1493) can be observed after only 2 h of ball milling (Fig. 1b) and the diffraction peak intensities of the starting materials, Fe_2O_3 and $\text{La}_2\text{O}_3/\text{La}(\text{OH})_3$, decreased, indicating the consumption of the starting materials. However, the diffraction peaks corresponding to La_2O_3 , $\text{La}(\text{OH})_3$, and Fe_2O_3 did not disappear completely at this ball milling time scale, suggesting the formation of LaFeO_3 has only partially taken place. On the other hand, the diffraction peak broadening suggested that there is a decrease in the average particle size of the starting materials. The particle sizes of Fe_2O_3 , La_2O_3 , and $\text{La}(\text{OH})_3$ were estimated to be 25.2, 8.3, and 11.4 nm, respectively. These suggest that the ball milling process can decrease the particle size and cause the formation of LaFeO_3 simultaneously. The co-existence of La_2O_3 and $\text{La}(\text{OH})_3$ phases during milling processes also suggests that either phase can be used as starting material to form the LaFeO_3 perovskite.

After 4 h of ball milling time, the intensities of LaFeO_3 diffraction peaks increase dramatically, while the diffraction peaks corresponding to the starting materials Fe_2O_3 and $\text{La}_2\text{O}_3/\text{La}(\text{OH})_3$ can still be seen, but with much weaker intensities, indicating the progress in the formation of the LaFeO_3 phase and continuous consumption of reactants. After 8 h of milling time, a trace of $\text{La}(\text{OH})_3$ phase is still present, which is in good agreement with the fact that the La_2O_3 is highly hygroscopic. The highly dispersed La_2O_3 phase can absorb moisture and turns into $\text{La}(\text{OH})_3$ easily, such that no La_2O_3 phase can be detected. At 8 h of milling time, the main crystalline phase is LaFeO_3 . Continuous ball milling up to 12 h increases the average particle size of LaFeO_3 phase, which can be confirmed by the increase in diffraction peak intensities of the LaFeO_3 phase (Fig. 1e). This indicates the possible formation of agglomerates of fine LaFeO_3 particles. On the other hand, the LaFeO_3 phase is the only detectable crystalline phase, no second phase was observed, indicating the mechanochemical activation method through ball milling of $\text{La}_2\text{O}_3/\text{La}(\text{OH})_3$ and Fe_2O_3 with stoichiometric ratio for 12 h can be employed to synthesize the LaFeO_3 -based perovskite material of single phase. Lattice parameters for the formed LaFeO_3 phase obtained from Rietveld refinement have values of $a = 5.5592 \text{ \AA}$, $b = 5.5875 \text{ \AA}$, $c = 7.8499 \text{ \AA}$, and unit cell volume $V = 243.84 \text{ \AA}^3$, suggesting the resulting products are crystallized in the orthorhombic system with an ABO_3 -type perovskite structure. The average particle size of LaFeO_3 single phase was estimated to be $\sim 17.5 \text{ nm}$.

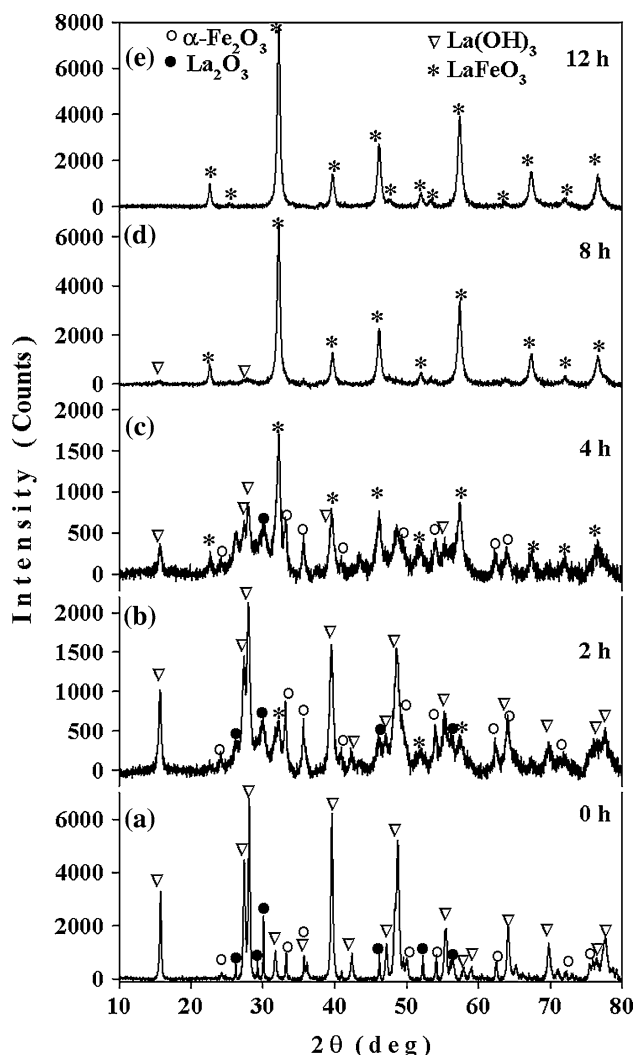


Fig. 1 XRPD patterns of mixed La_2O_3 – $\alpha\text{-Fe}_2\text{O}_3$ sample with 1:1 molar ratio at ball milling time of: (a) 0 h; (b) 2 h; (c) 4 h; (d) 8 h; (e) 12 h, respectively

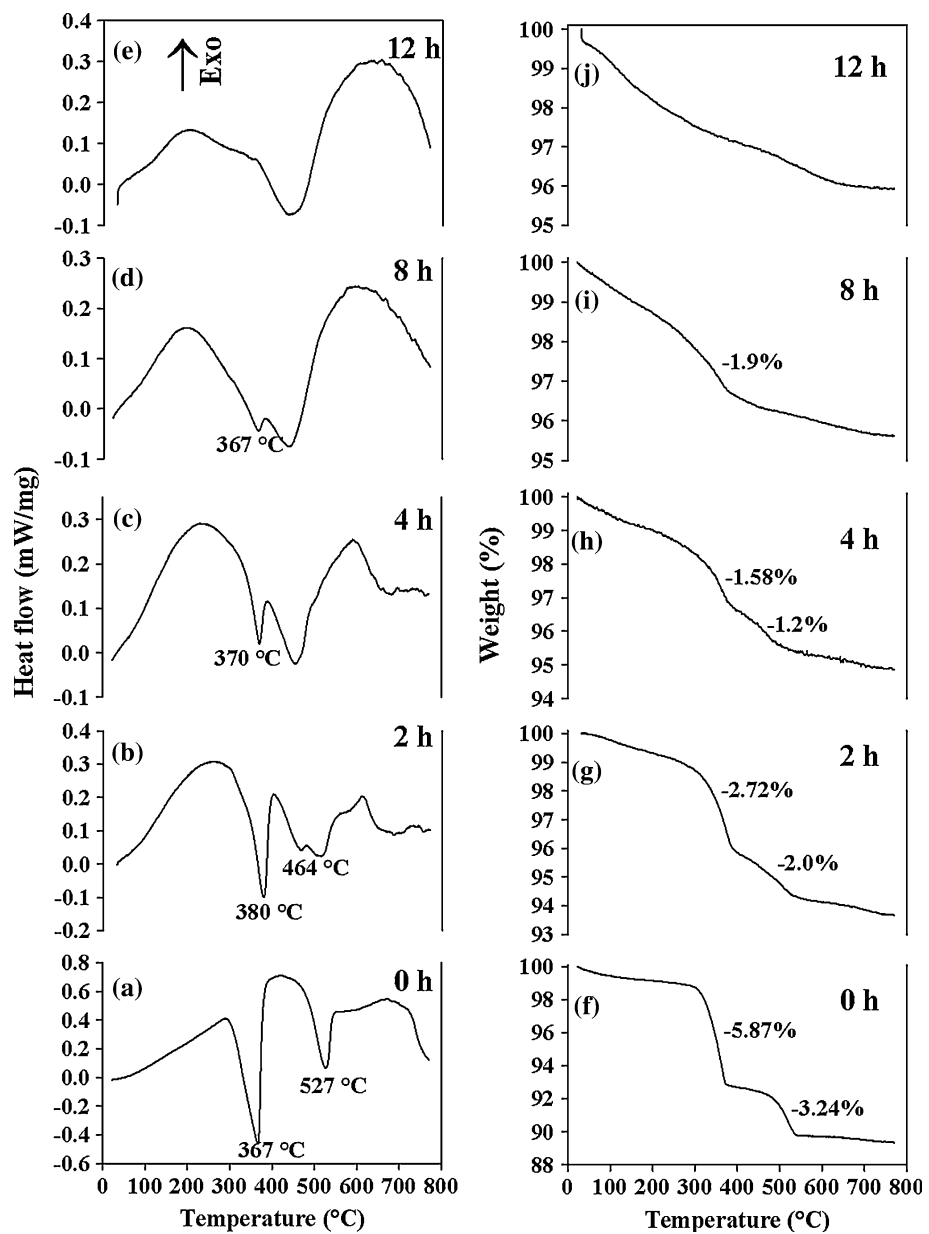
Simultaneous DSC–TGA

TG–DTA experiments have been widely used to study thermal behavior of precursors of the LaFeO₃ perovskite-type composite oxides nanocrystals [24, 25], and DTA was also employed to study the thermal behavior of Fe₂O₃ + 3Al + Fe powder mixture under different ball milling times [26]. It was found that the ball milling process has a great effect on the thermal behavior of the mixed oxide systems and nanocomposite powders.

Figure 2 displays the simultaneous DSC–TGA curves of mixed starting materials after different ball milling times. For 0 h ball-milled sample, two endothermic peaks can be clearly observed from the DSC measurement (Fig. 2a), with

the peak temperatures at 367 and 527 °C, respectively. The thermal behavior of the 0 h ball-milled sample was simultaneously investigated using TGA analysis. As can be seen in Fig. 2f, the thermogravimetry reveals two major weight losses for this sample: one is in a relatively low temperature range from 300 to 385 °C, with a weight loss of –5.87%; and the other starts at 450 °C and ends at 530 °C, with a weight loss of –3.24%. These two weight losses are due to the dehydration of La(OH)₃, which was formed when La₂O₃ was exposed to air and absorbed moisture. These two weight losses are in good agreement with the DSC curve of this sample (Fig. 2a), which shows two endothermic peaks. The peak temperatures of 367 and 527 °C are exactly at the center of TGA curve where the two weight losses occur.

Fig. 2 DSC curves of mixed La₂O₃–α-Fe₂O₃ sample with 1:1 molar ratio at ball milling time of: (a) 0 h; (b) 2 h; (c) 4 h; (d) 8 h; (e) 12 h, and TGA curves of mixed La₂O₃–α-Fe₂O₃ sample with 1:1 molar ratio at ball milling time of: (f) 0 h; (g) 2 h; (h) 4 h; (i) 8 h; (j) 12 h



XRPD analysis of the residue of the 0 h ball-milled sample after DSC–TGA measurements shows there is no detectable LaFeO_3 phase after heat treatment up to 800 °C. Therefore, the wide exothermic band on the DSC curve of the 0 h ball-milled La_2O_3 – Fe_2O_3 sample in the studied temperature range can be assigned to the crystallization of the starting materials under heat treatment.

As the milling progresses, the intensities of the endothermic peaks decrease, and the weight loss values decrease as well. After 2 h of milling time, the two endothermic peaks can still be seen (Fig. 2b), with the peak temperatures at 380 and 464 °C, respectively. The TGA curve (Fig. 2g) shows two corresponding weight losses, with the values of –2.72 and –2.0%, respectively. The decrease in weight loss values is due to the consumption of La_2O_3 and La(OH)_3 to form LaFeO_3 after ball milling. This is confirmed by the XRPD results, which show that the intensities of La(OH)_3 diffraction peaks decrease with the increase in ball milling time and part of the $\text{La}_2\text{O}_3/\text{La(OH)}_3$ reacted with Fe_2O_3 to form LaFeO_3 perovskite. The formed single phase LaFeO_3 perovskite does not absorb moisture as easily as La_2O_3 does, which can be confirmed from the DSC curve of 12 h ball-milled sample (Fig. 2e). There is no endothermic peak corresponding to the dehydration of La(OH)_3 and no sharp decrease in weight percentage can be observed either (Fig. 2j). The variation in weight for this 12 h ball-milled sample is due to the thermal shift in weight under heat treatment, and the two broad bands (from 35 to 441 °C, and from 441 to 800 °C) in DSC curve (Fig. 2e) are due to the crystallization and re-crystallization of the formed nano-sized LaFeO_3 phase.

Mössbauer spectroscopy

The three Mössbauer parameters, isomer shift, quadrupole splitting, and hyperfine magnetic field can provide important information about a particular compound with atomic resolution scale. The isomer shift provides direct information about the electron density at nucleus. The quadrupole splitting reflects the interaction between the nuclear quadrupole and the surrounding electric field gradient, and the magnetic hyperfine field gives an indication about the interaction between the nucleus and any surrounding magnetic fields. The combination of XRPD and Mössbauer spectroscopy provides more detail about the growth mechanism of LaFeO_3 -based perovskite, such as average particle size, inequivalent site of iron, and transition metal ion substitution of Fe^{3+} in Fe_2O_3 lattice.

Figure 3a–e shows the room temperature transmission Mössbauer spectra of mixed La_2O_3 – $\alpha\text{-Fe}_2\text{O}_3$ oxides (1:1 molar ratio) after ball milling for 0, 2, 4, 8, and 12 h, respectively. The hyperfine parameters corresponding to these spectra are given in Table 1. At 0 h of milling time,

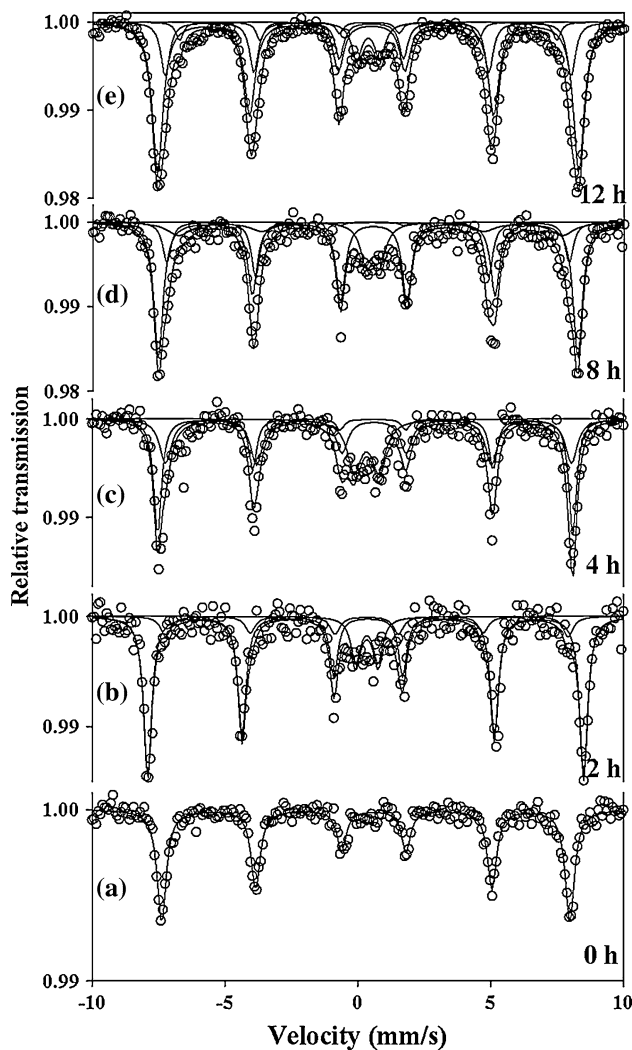


Fig. 3 Mössbauer spectra of mixed La_2O_3 – $\alpha\text{-Fe}_2\text{O}_3$ sample with 1:1 molar ratio at ball milling time of: (a) 0 h; (b) 2 h; (c) 4 h; (d) 8 h; (e) 12 h, respectively

the spectrum was fitted with one sextet (Fig. 3a), corresponding to $\alpha\text{-Fe}_2\text{O}_3$. After 2 h of milling, the Mössbauer spectrum was fitted with two sextets and one doublet, indicating the La^{3+} substitution of Fe^{3+} in the $\alpha\text{-Fe}_2\text{O}_3$ lattice and the formation of LaFeO_3 phase; the relative abundance of a magnetic phase with highest hyperfine field (50.88 T) is 73.88%, and the relative population of a magnetic phase with a low hyperfine field of 46.98 T is 14.43%. Due to the overlapped Mössbauer spectra of $\alpha\text{-Fe}_2\text{O}_3$ and formed LaFeO_3 phase, it is very difficult to determine the exact percentages of $\alpha\text{-Fe}_2\text{O}_3$, La^{3+} substituted $\alpha\text{-Fe}_2\text{O}_3$, and LaFeO_3 phases individually. The small doublet, with isomer shift and quadrupole splitting values of 0.3448 and 0.8388 mm/s, respectively, has a population of 11.69%, and can be assigned to the nano-sized LaFeO_3 particles with superparamagnetic properties. The formation

Table 1 Mössbauer parameters for mixed $\text{La}_2\text{O}_3-\alpha\text{-Fe}_2\text{O}_3$ with 1:1 molar ratio at different ball milling times

BMT (h)	I.S. (mm/s)	Q.S. (mm/s)	B (T)	Abundance (%)
0	0.4560	−0.3013	47.64	100
2	0.3491	−0.0930	50.88	73.88
	0.3449	−0.0075	46.98	14.43
	0.3448	0.8388	—	11.69
4	0.4283	−0.2907	48.46	38.32
	0.5140	−0.2096	47.39	41.43
	0.3295	0.9165	—	19.87
8	0.4605	−0.2099	48.94	59.03
	0.4271	−0.1507	46.96	18.52
	0.4860	−0.0862	44.77	12.17
	0.5403	0.5066	—	10.27
12	0.4258	−0.1306	49.17	61.62
	0.4212	−0.1219	47.38	23.93
	0.3808	−0.0399	44.04	7.06
	0.3611	0.8711	—	7.39
Error	±0.002	±0.004	±0.1	±0.01

BMT ball milling time, I.S. isomer shift (relative to the source), Q.S. quadrupole splitting/shift, B hyperfine magnetic field

of nano-sized LaFeO_3 has been confirmed from the broad XRPD diffraction peaks of LaFeO_3 phase (Fig. 1b).

After 8 h of milling time, the spectrum was fitted with three sextets and one quadrupole split doublet. From the XRPD pattern (Fig. 1d) of this sample, the LaFeO_3 magnetic phase was the dominant phase with a trace of the $\text{La}(\text{OH})_3$ phase, and no Fe_2O_3 phase was observed. Therefore, these three sextets can be assigned to the LaFeO_3 phase with hyperfine magnetic fields of 48.94, 46.96, and 44.77 T, respectively. Similar to the 4 h ball-milled sample, the doublet, with a quadrupole splitting of 0.5066 mm/s and an isomer shift of 0.5403 mm/s, respectively, can be assigned to the superparamagnetic nano-sized LaFeO_3 particles. In addition, the population of this quadrupole splitting doublet component decreases from 19.87% for 4 h milling to 10.27% for 8 h milling, indicating the formation of agglomerates of LaFeO_3 nanoparticles. Indeed, the relative abundance of this superparamagnetic phase decreases from 10.27% for 8 h milling to 7.39% for 12 h milling. Similar to the 8 h ball-milled sample, the three sextets in the Mössbauer spectrum of 12 h ball-milled sample can also be assigned to the LaFeO_3 phase, with hyperfine magnetic fields of 49.17, 47.38, and 44.04 T, respectively, corresponding to the LaFeO_3 phase with various particle sizes. The abundance of the magnetic phase with higher magnetic hyperfine field increases with the ball milling time, suggesting that a longer ball milling time leads to the

formation of well-crystallized LaFeO_3 phase from nano-sized particles. This is also confirmed by the XRPD results that the diffraction peak intensities of crystallized LaFeO_3 phase increase with the ball milling time.

It has been reported that the Mössbauer spectra of LaFeO_3 can be fitted with different sets of sextets and doublets due to the wide distribution of LaFeO_3 particle size [27]. LaFeO_3 crystallites prepared by the citrate method with size of 70 nm possessed an antiferromagnetic structure and only one sextet was needed for its Mössbauer spectrum, while that of 12 nm particles was the superposition of the weaker antiferromagnetic structure and the stronger superparamagnetic structure, such that the broadened sextets and doublets were needed [27]. However, the weak ferromagnetic behavior for LaFeO_3 with particle sizes of 30 and 40 nm was also observed from the hysteresis measurements [12, 15]. The Mössbauer spectrum of the LaFeO_3 single phase prepared by mechanical milling method was also reported to be composed of a broadened sextet pattern and a broadened singlet [28] and the average hyperfine magnetic field was lower than that of the bulk LaFeO_3 [29]. All these suggest that the Mössbauer spectra of LaFeO_3 materials can be fitted with different sets of sextets and doublets due to the different preparation methods which lead to different distribution in particle sizes. The orthorhombic symmetry of the formed LaFeO_3 phase with lattice parameters $a \neq b \neq c$, and the defects of LaFeO_3 crystallites under ball milling may also account for the different sets of sextets.

Further analysis of the XRPD patterns and Mössbauer spectra of mixed $\text{La}_2\text{O}_3-\text{Fe}_2\text{O}_3$ samples with different molar ratios (1:9, 3:7, 7:3) at different ball milling times was performed. It was found that the doublet in Mössbauer spectra appears simultaneously with the formation of the LaFeO_3 phase, no doublet exists when there is no detectable LaFeO_3 phase, suggesting the doublet is arising from the superparamagnetic nano-sized LaFeO_3 particles and not from the nonmagnetic phase in which the Fe^{3+} substitution of La^{3+} in La_2O_3 or $\text{La}(\text{OH})_3$ lattices occurs. Therefore, the growth mechanism of LaFeO_3 perovskite through ball milling method may follow these steps: first of all, the particle sizes of starting materials $\text{La}_2\text{O}_3/\text{La}(\text{OH})_3$ and Fe_2O_3 are decreased to less than 10 nm under the ball milling process; secondly, La^{3+} substitution of Fe^{3+} in the Fe_2O_3 lattice occurs, which can be identified by the Mössbauer spectra with multiple sextets; the formation of nano-sized LaFeO_3 particle with superparamagnetic properties; at last, further ball milling process introduces the completion of La^{3+} substitution of Fe^{3+} in Fe_2O_3 lattice and the formation of the LaFeO_3 single phase with well-developed ABO_3 -type perovskite crystalline structure and different particle sizes.

Scanning electron microscopy

SEM was employed to study the morphology and particle size of the as-obtained products. Figure 4 shows secondary electron SEM images at different magnifications of the as-obtained LaFeO_3 perovskite through 12 h ball milling of the starting materials. A mixture of large crystal agglomerates in the size range 1–30 μm coated with much finer particles with nanometer dimensions are observed. Several agglomerates with 10–20 μm in size can be seen (Fig. 4a). However, most particles are still less than 10 μm at this magnification scale. Figure 4b shows more details of the as-obtained LaFeO_3 perovskite at a different magnification. It can be seen clearly that the large agglomerates consist of fine particles with redundant sizes in nanometer range. Particles in the nanometer size range are distributed randomly on the edge and top of the big agglomerates, indicating ball milling is a useful method to prepare LaFeO_3 perovskite as nanoparticles. The as-obtained LaFeO_3 perovskite has a wide-range distribution in particle size diameters, consisting of nanometer-sized particles to micrometer-sized agglomerates. This is in good agreement with Mössbauer results, which show different sets of sextets and doublet. Agglomerates in micrometer size range were also found in In_2O_3 and Ta_2O_5 mixture milled for 4 h [30], indicating it is a general phenomenon to produce some agglomerates with micrometer size using the high energy ball milling method.

Optical diffuse reflectance spectroscopy

The optical diffuse reflectance spectra for samples Fe_2O_3 , lanthanum oxide, and $\text{La}_2\text{O}_3-\alpha\text{-Fe}_2\text{O}_3$ (1:1 molar ratio) with different ball milling times are shown in Fig. 5. For Fe_2O_3 , the valence and conduction bands arise from crystal field splitting of the Fe $3d$ levels due to the octahedral coordination of oxygen around Fe [31]. As

shown in Fig. 5a, diffuse reflectance spectra of original Fe_2O_3 exhibit a band gap energy value of ~ 2.2 eV, which is consistent with the reported value for bulk

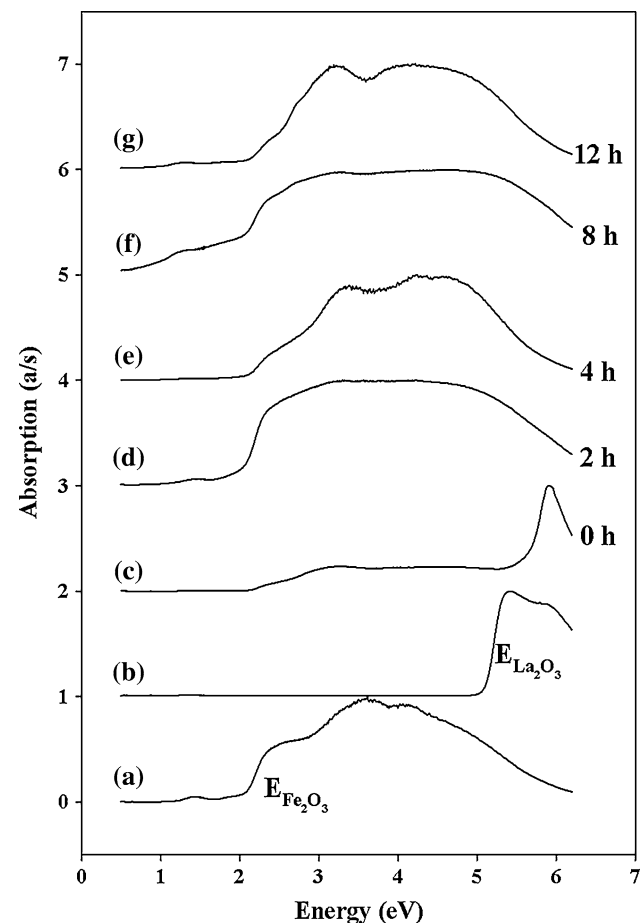


Fig. 5 The normalized optical diffuse reflectance spectrum converted to absorption for samples: (a) original hematite, (b) original lanthanum oxide, and mixed $\text{La}_2\text{O}_3-\alpha\text{-Fe}_2\text{O}_3$ sample with 1:1 molar ratio at ball milling time of: (c) 0 h; (d) 2 h; (e) 4 h; (f) 8 h; (g) 12 h, respectively. On the y-axis, α is the absorbance and s is the scattering coefficient constant

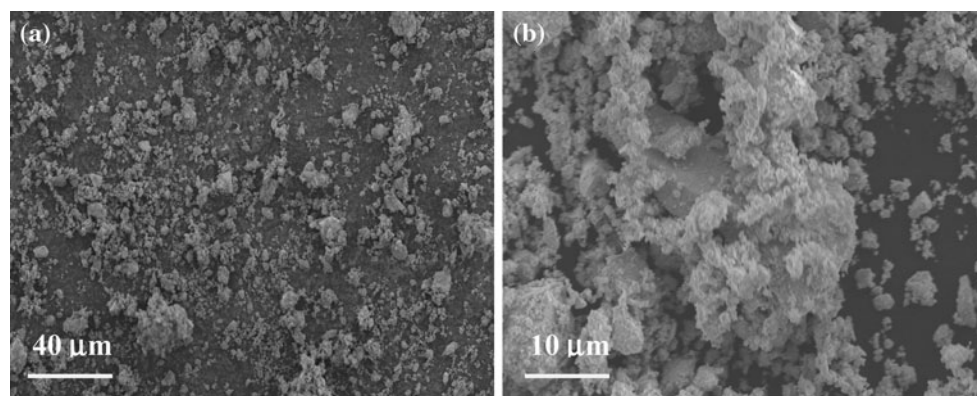


Fig. 4 SEM images of mixed $\text{La}_2\text{O}_3-\alpha\text{-Fe}_2\text{O}_3$ sample with 1:1 molar ratio at ball milling time of 12 h with different magnifications

hematite [32, 33]. Lanthanum(III) oxides have a structure in which lanthanum is sevenfold coordinated, with four short La–O bonds (2.30 Å) and three longer La–O bonds (2.70 Å). The band gap of La_2O_3 is indirect, and it has recently been reported in the range from 4.3 to 6.0 eV [34, 35]. The valence band is at Γ and about 3.5 eV wide. The conduction band minimum is due to the La d states. The density of state of La_2O_3 shows that the valence band is strongly localized on O p states and the conduction band on La d with some La s , p states starting at 8 eV [34]. The measured band gap energy of the lanthanum oxide has a value of \sim 5.2 eV, the difference in band gap energy may arise from the co-existence of La_2O_3 and La(OH)_3 phases which has been confirmed from XRPD measurement or for surface modification of La_2O_3 during the physically mixing process. For sample La_2O_3 – α - Fe_2O_3 (1:1 molar ratio) with 0 h of milling time, in other words, just after that hematite–lanthanum oxides are physically mixed, the band gap energy of Fe_2O_3 and lanthanum oxide shifts to higher energy levels, with values of \sim 2.7 eV and \sim 5.76 eV, respectively. The variations in band gap energies of Fe_2O_3 and lanthanum oxide are attributed to the change in density of states of $2p$ level for O and $3d$ level for La and Fe. A similar change in band gap energy was also observed for Fe-doped TiO_2 system [36].

After 2 h of milling time, the band gap energy of the resulted sample is \sim 2.23 eV, which is slightly higher than that of original Fe_2O_3 and lower than that of 0 h ball-milled hematite–lanthanum oxide sample. It is hard to determine the exact change in band gap energy of original Fe_2O_3 due to the similar band gap energies of Fe_2O_3 and formed LaFeO_3 perovskite [37]. The band gap energy of the LaFeO_3 phase is also ascribed to the electronic transitions from the valence band to conduction band ($\text{O}_{2p} \rightarrow \text{Fe}_{3d}$, \sim 2.52 eV). No obvious band gap for La_2O_3 was observed due to the absorbent coefficients falling down and it is very small in the wavelength range of UV–Vis light. Therefore, the change in band gap energies of ball-milled samples at different ball milling times is mainly due to the decrease in particle size, the gradual La^{3+} substitution of Fe^{3+} in Fe_2O_3 lattice, and the formation of LaFeO_3 perovskite phase during milling process, respectively. The band gap energy of the as-obtained LaFeO_3 single phase is \sim 2.67 eV (Fig. 5g); in addition, it can be ascertained that the as-obtained LaFeO_3 samples can be excited by the light with the wavelength of equal to or smaller than 468 nm. This means the simple, low cost ball milling method can be used to tune the band gap energy by adjusting ball milling time and molar ratio of mixed oxides, which have importance in photocatalytic fuel production.

Conclusions

Single phase LaFeO_3 perovskite was synthesized mechanochemically through ball milling of La_2O_3 and Fe_2O_3 in stoichiometric ratios at room temperature. La_2O_3 was highly hygroscopic and absorbed moisture to partially form the La(OH)_3 phase after being exposed to air, such that La_2O_3 and La(OH)_3 phases coexist in the ball milling process. There is no preference for phases La_2O_3 or La(OH)_3 when forming the LaFeO_3 . The formation of LaFeO_3 perovskite was found after only 2 h of ball milling, and the amount of LaFeO_3 gradually increased with the ball milling time. After 12 h of ball milling, single phase LaFeO_3 was formed. The Mössbauer spectroscopy studies indicated that the spectrum of the formed LaFeO_3 phase consisted of three sextets and one doublet, indicating that LaFeO_3 has different particle sizes and possible defects. It also indicated some nano-sized LaFeO_3 particles possess superparamagnetic properties. SEM images of the formed LaFeO_3 perovskite confirmed the wide-range distribution of particles sizes, from nanometer-sized particles to micrometer-sized agglomerates. Further analysis of Mössbauer spectra showed the formation of the LaFeO_3 phase was primarily caused by the La^{3+} substitution of Fe^{3+} in Fe_2O_3 lattice as an intermediate. Optical diffuse reflectance spectroscopy studies show that the formed LaFeO_3 phase has semiconductor properties, with the band gap energy of \sim 2.67 eV.

Acknowledgement This work was supported by the National Science Foundation under grant DMR-0854794.

References

1. Tejua LG, Fireo JL, Tascón JMD (1989) Adv Catal 36:237
2. Yamazoe N, Teraoka Y (1990) Catal Today 8:175
3. Arakawa T, Kurachi H, Shiokawa J (1985) J Mater Sci 4:1207. doi:[10.1007/BF01026315](https://doi.org/10.1007/BF01026315)
4. Traversa E, Matsushima S, Okada G, Sadaoka Y, Sakai Y, Watanabe K (1995) Sens Actuators B 25:661
5. Asamitsu A, Moritomo Y, Tomioka Y, Arima T, Tokura Y (1995) Nature 373:407
6. Yao T, Ariyoshi A, Inui T (1997) J Am Ceram Soc 80:2441
7. Kindermann L, Das D, Nickel H, Hilpert K, Appel CC, Poulson FW (1997) J Electrochem Soc 144:717
8. Stevenson JW, Armstrong TR, Carneim RD, Pederson LR, Weber WJ (1996) J Electrochem Soc 143:2722
9. Cherry M, Islam MS, Catlow CRA (1995) J Solid State Chem 118:125
10. Belessi VC, Trikalitis PN, Ladavos AK, Bakas TV, Pomonis PJ (1999) Appl Catal A 177:53
11. Popa M, Frantti J, Kakihana M (2002) Solid State Ionics 154:437
12. Popa M, Moreno JMC (2011) J Alloys Compd 509:4108
13. Kondakindi RR, Kundu A, Karan K, Peppley BA, Qi AD, Thurgood C, Schurer P (2010) Appl Catal A 390:271

14. Vázquez-Vázquez C, Kögerler P, López-Quintela MA, Sánchez RD, Rivas J (1998) *J Mater Res* 13:451
15. Sivakumar M, Gedanken A, Zhong W, Jiang YH, Du YW, Brukental I, Bhattacharya D, Yeshurun Y, Nowik I (2004) *J Mater Chem* 14:764
16. Giannakas AE, Ladavos AK, Pomonis PJ (2004) *Appl Catal B* 49:147
17. Li KY, Wang DJ, Wu FQ, Xia TF, Li TJ (1999) *Mater Chem Phys* 60:226
18. Zhang QW, Saito F (2001) *J Mater Sci* 36:2287. doi:[10.1023/A:1017520806922](https://doi.org/10.1023/A:1017520806922)
19. Cristóbal AA, Botta PM, Bercoff PG, Port López JM (2009) *Mater Res Bull* 44:1036
20. Petrović S, Terlecki-Barićević A, Karanović Lj, Kirilov-Stefanov P, Zdujić M, Dondur V, Paneva D, Mitov I, Rakić V (2008) *Appl Catal B* 79:186
21. Kaliaguine S, Van Neste A, Szabo V, Gallot JE, Bassir M, Muzychuk R (2001) *Appl Catal A* 209:345
22. Nakayama S (2001) *J Mater Sci* 36:5643. doi:[10.1023/A:1012526018348](https://doi.org/10.1023/A:1012526018348)
23. Kubelka P, Munk F (1931) *Z Tech Phys* 12:593 (trans: Westin S)
24. Li F, Zheng HG, Xia DZ, Xin XQ, Xue ZL (2002) *Mater Lett* 53:282
25. Wang YP, Zhu JW, Zhang LL, Yang XJ, Lu LD, Wang X (2006) *Mater Lett* 60:1767
26. Khodaei M, Enayati MH, Karimzadeh F (2008) *J Mater Sci* 43:132. doi:[10.1007/s10853-007-2123-7](https://doi.org/10.1007/s10853-007-2123-7)
27. Li X, Cui XH, Liu XW, Jin MZ, Xiao LZ, Zhao MY (1991) *Hyperfine Interact* 69:851
28. Berry FJ, Ren XL, Grancedo JR, Marco JF (2004) *Hyperfine Interact* 156–157:335
29. Eibschütz M, Shtrikman S, Treves D (1967) *Phys Rev* 156:562
30. Tojo T, Zhang QW, Saito F (2008) *J Mater Sci* 43:2962. doi:[10.1007/s10853-006-1472-y](https://doi.org/10.1007/s10853-006-1472-y)
31. Morin FJ (1954) *Phys Rev* 93:1195
32. Marusak LA, Messier R, White WB (1980) *J Phys Chem Solids* 41:981
33. Dare-Edwards MP, Goodenough JB, Hamnett A, Trevellick PR (1983) *J Chem Soc Faraday Trans* 79:2027
34. Robertson J, Peacock PW (2005) Atomic structure, interfaces, and defects of high dielectric constant gate oxides. In: Demkov AA, Navrotsky AA (eds) Materials fundamentals of gate dielectrics. Springer, Netherland, p 183
35. Cheng JB, Li AD, Shao QY, Ling HQ, Wu D, Wang Y, Bao YJ, Wang M, Liu ZG, Ming NB (2004) *Appl Surf Sci* 233:91
36. Thimsen E, Biswas S, Lo CS, Biswas P (2009) *J Phys Chem C* 113:2014
37. Li SD, Jing LQ, Fu W, Yang LB, Xin BF, Fu HG (2007) *Mater Res Bull* 42:203